Available online at www.sciencedirect.com
ScienceDirect
Geochimica et Cosmochimica Acta 72 (2008) 3431–3445
Geochimica et Cosmochimica Acta
www.elsevier.com/locate/gca

Surface complexation effects on phosphate adsorption to ferric iron oxyhydroxides along pH and salinity gradients in estuaries and coastal aquifers

Claudette Spiteri *, Philippe Van Cappellen, Pierre Regnier

Faculty of Geosciences, Department of Earth Sciences - Geochemistry, Utrecht University, P.O. Box 80021, 3508 TA Utrecht, The Netherlands

Received 3 July 2007; accepted in revised form 5 May 2008; available online 16 May 2008

Abstract

Non-conservative behavior of dissolved inorganic phosphate (DIP) in estuaries is generally ascribed to desorption from iron and aluminum (hydr)oxides with increasing salinity. Here, we assess this hypothesis by simulating the reversible adsorption of phosphate onto a model oxide (goethite) along physico-chemical gradients representative of surface and subsurface estuaries. The simulations are carried out using a surface complexation model (SCM), which represents the main aqueous speciation and adsorption reactions of DIP, plus the ionic strength-dependent coulombic interactions in solution and at the mineral–solution interface. According to the model calculations, variations in pH and salinity alone are unlikely to explain the often reported production of DIP in surface estuaries. In particular, increased aqueous complexation of phosphate by Mg^{2+} and Ca^{2+} ions with increasing salinity is offset by the formation of ternary Mg-phosphate surface complexes and the drop in electrical potential at the mineral–water interface. However, when taking into account the downstream decrease in the abundance of sorption sites, the model correctly simulates the observed release of DIP in the Scheldt estuary. The sharp increase in pH accompanying the admixing of seawater to fresh groundwater should also cause desorption of phosphate from iron oxyhydroxides during seawater intrusion in coastal aquifers. As for surface estuaries, the model calculations indicate that significant DIP release additionally requires a reduction in the phosphate sorption site density. In anoxic aquifers, this can result from the supply of seawater sulfate and the subsequent reductive dissolution of iron oxyhydroxides coupled to microbial sulfate reduction.

1. INTRODUCTION

Sorption of dissolved inorganic phosphate (DIP) to soil and sediment particles, commonly at the surfaces of iron and aluminum (hydr)oxides, greatly limits its mobility (e.g., Krom and Berner, 1980; Frossard et al., 1995), and is, therefore, a crucial process in controlling phosphate availability to the biosphere. Although DIP behavior has been extensively studied in a variety of environments, both terrestrial and aquatic, comprehensive models of its fate and transport are still lacking. This is particularly true for environments that exhibit strong physico-chemical gradients, such as surface estuaries or the mixing zones in coastal aquifers known as subterranean estuaries (Moore, 1999). Such systems are characterized by large variations in pH, ionic strength and solution composition, all of which can influence the sorption of phosphate.

Field studies of phosphate dynamics along surface estuarine salinity gradients (e.g., Froelich, 1988; Lebo, 1991; Paludan and Morris, 1999; Sundareshwar and Morris, 1999; Van der Zee et al., 2007), as well as laboratory studies (e.g., Carritt and Goodgal, 1954; Carpenter and Smith, 1984; Fox et al., 1986; Gardolinski et al., 2004), indicate non-conservative behavior of phosphate during mixing of

* Corresponding author. Present address: Marine and Coastal Systems, Deltares (WL — Delft Hydraulics), P.O. Box 177, 2600 MH Delft, The Netherlands. Fax: +31 15 285 85 82.
E-mail address: claudette.spiteri@deltares.nl (C. Spiteri).

0016-7037/$ - see front matter © 2008 Elsevier Ltd. All rights reserved.
doi:10.1016/j.gca.2008.05.003

freshwater and seawater, leading to higher DIP concentrations than those expected from conservative mixing alone. Likewise, Nyvang (2003) reported a significant increase in the DIP concentration upon seawater intrusion in a shallow aquifer along the Danish coast. The observed increase of DIP was attributed to the effects of pH, ionic strength and changes in solution composition brought about by freshwater–seawater mixing. In particular, the author proposed that the competition between phosphate and sulfate ions for sorption sites was in part responsible for the release of DIP.

Sorption of inorganic phosphate is expected to vary along estuarine salinity gradients, partly because the surface charging properties of common metal (hydr)oxides are significantly different under typical freshwater and seawater conditions (Barrow et al., 1980). In order to model phosphate sorption under conditions of variable solution composition, surface complexation models (SCMs) are particularly suitable (Davis and Kent, 1990; Dzombak and Morel, 1990; Stumm, 1992; Antelo et al., 2005). However, so far SCMs have mainly been applied to phosphate adsorption studies performed at constant ionic strength and background electrolyte composition, (e.g., Sigg and Stumm, 1981; Hawke et al., 1989; Hiemstra and Van Riemsdijk, 1996; Stollenwerk, 1996; Gao and Mucci, 2001, 2003). Qualitatively, the SCMs predict that phosphate desorbs from metal oxyhydroxides as pH increases (Sigg and Stumm, 1981; Goldberg and Sposito, 1984; Hawke et al., 1989; Geelhoed et al., 1997; Gao and Mucci, 2001, 2003).

In this study, we apply a SCM to describe the adsorption of phosphate to the model oxide goethite, along the transition from freshwater to seawater in surface and subterranean mixing regimes. We begin by reproducing the results of the adsorption experiments of Gao and Mucci (2001, 2003), performed in 0.7 M NaCl solution and artificial seawater. Next, the speciation calculations for the aqueous solution and mineral surface are extended to low ionic strength (0.001 M) conditions. The model is then used to interpret the measured DIP and sorbed inorganic phosphate (SIP) distributions along the salinity gradient in the Scheldt estuary (Belgium/The Netherlands) (Van der Zee et al., 2007). Finally, the SCM is coupled to a 2D density-dependent groundwater flow model to explore the effect of saltwater intrusion on phosphate mobilization in a coastal aquifer setting. The model results provide new insight into the mechanisms responsible for the non-conservative behavior of DIP typically observed along the land-to-ocean transition.

2. MODEL SETUP

2.1. Aqueous and mineral surface speciation

The SCM describes the adsorption of phosphate on goethite (FeO(OH)), the most common and stable crystalline iron (hydr)oxide in soils and sediments (e.g., Cornell and Schwertmann, 2003; Van der Zee et al., 2003). The SCM developed in the present study follows closely the work of Gao and Mucci (2001, 2003). Details on the experimental procedures can be found therein. In particular, we use their phosphate adsorption data and constant capacitance model (CCM) parameter values obtained for goethite in 0.7 M NaCl and artificial seawater solutions. Although other data sets describe phosphate adsorption to ferric iron oxyhydroxides (e.g., Dzombak and Morel, 1990), the experimental results of Gao and Mucci are the most relevant for complex estuarine solutions. Furthermore, these authors consider an extensive reaction network to interpret their data, including the formation of ternary surface complexes with seawater cations. As discussed below, the latter may play a major role during estuarine mixing.

The SCM model considers 13 aqueous and 12 surface species (Table 1), taking into account the dissociation of phosphoric acid, the formation of aqueous complexes with the major cations (Na^+, Ca^{2+}, Mg^{2+}) present in natural waters, the protonation–deprotonation reactions of the surface sites of goethite, and the formation of phosphate, Ca^{2+} and Mg^{2+} surface complexes. Also included are ternary surface complexes, for example, $\equiv FeOMgHPO_4^-$. The formation of these ternary surface complexes is triggered by the binding of divalent aqueous cations to the negatively-charged goethite surface under alkaline conditions, thereby facilitating further adsorption of aqueous phosphate anions (Gao and Mucci, 2003). The set of 19 equilibrium reactions included in the model, plus their respective intrinsic stability constants, are listed in Tables 2 and 3. The intrinsic stability constants are calculated from the apparent equilibrium constants obtained by Gao and Mucci (2001, 2003) in high ionic strength solutions ($I = 0.7$ M), using Davies equation (Davies, 1938) to estimate the activity coefficients of the aqueous species. Although the use of Davies equation at ionic strengths higher than 0.1 M is questionable (e.g., Morel and Hering, 1993), the predicted activity coefficients closely agree with values derived from Pitzer's equations or related models (Millero, 1982; Millero and Schreiber, 1982).

The mole balance equation for total phosphate (Ptotal) in the model is:

$$\begin{aligned}\text{Ptotal} = {} & [H_2PO_4^-] + [HPO_4^{2-}] + [PO_4^{3-}] + [NaH_2PO_4^0] \\ & + [NaHPO_4^-] + [NaPO_4^{2-}] + [MgHPO_4^0] \\ & + [CaHPO_4^0] + [CaPO_4^-] + [\equiv FePO_4^{2-}] \\ & + [\equiv FePO_4H^-] + [\equiv FePO_4H_2] \\ & + [\equiv FeOMgHPO_4^-] + [\equiv FeOMgH_2PO_4^0] \\ & + [\equiv FeOCaHPO_4^-] + [\equiv FeOCaH_2PO_4^0] \qquad (1)\end{aligned}$$

and that for the total number of surface sites (Stotal) is:

Table 1
Species included in the model

Aqueous species	Surface species
H^+	$\equiv FeOH$, $\equiv FeO^-$, $\equiv FeOH_2^+$
$H_2PO_4^{2-}$, HPO_4^{2-}, PO_4^{3-}	$\equiv FePO_4^{2-}$, $\equiv FePO_4H^-$, $\equiv FePO_4H_4^0$
Na^+, Mg^{2+}, Ca^{2+}	$\equiv FeOMg^+$, $\equiv FeOCa^+$
$NaH_2PO_4^0$, $NaHPO_4^-$, $NaPO_4^{2-}$	$\equiv FeOMgHPO_4^-$, $\equiv FeOMgH_2PO_4^0$
$MgHPO_4^0$, $CaHPO_4^0$, $CaPO_4^-$	$\equiv FeOCaHPO_4^-$, $\equiv FeOCaH_2PO_4^0$

Variables in italics are independent variables of the SCM. "≡" represents the mineral surface lattice.

Table 2
Reaction network for the SCM in NaCl electrolyte solution

Reaction	Log$K$ (25 °C)
$H_2PO_4^- \leftrightarrow H^+ + HPO_4^{2-}$	−7.18
$H_2PO_4^- \leftrightarrow 2H^+ + PO_4^{3-}$	−19.61
$Na^+ + H_2PO_4^- \leftrightarrow NaH_2PO_4^{3-}$	−0.22
$Na^+ + H_2PO_4^- \leftrightarrow NaHPO_4^- + H^+$	−6.51
$Na^+ + H_2PO_4^- \leftrightarrow NaPO_4^{2-} + 2H^+$	−18.06
Surface complexes	
$\equiv FeOH + H^+ \leftrightarrow \equiv FeOH_2^+$	7.61
$\equiv FeOH \leftrightarrow \equiv FeO^- + H^+$	−9.76
$\equiv FeOH + H_2PO_4^- \leftrightarrow \equiv 2FePO_4^{2-} + H^+ + H_2O$	0.7
$\equiv FeOH + H_2PO_4^- \leftrightarrow \equiv FePO_4H^- + H_2O$	7.99
$\equiv FeOH + H_2PO_4^- + H^+ \leftrightarrow \equiv FePO_4H_2^0 + H_2O$	12.78

All stability constants are *intrinsic* constants (modified from Gao and Mucci, 2001).

Table 3
Additional reactions for the SCM in complex electrolyte solution

Reaction	Log$K$ (25 °C)
$Mg^{2+} + H_2PO_4^- \leftrightarrow MgHPO_4^0 + H^+$	−4.42
$Ca^{2+} + H_2PO_4^- \leftrightarrow CaHPO_4^0 + H^+$	−4.65
$Ca^{2+} + H_2PO_4^- \leftrightarrow H_2CaPO_4^- + 2H^+$	−13.13
Surface complexes	
$\equiv FeOH + Mg^{2+} \leftrightarrow \equiv FeOMg^+ + H^+$	−3.43
$\equiv FeOH + Ca^{2+} \leftrightarrow \equiv FeOCa^+ + H^+$	−6.46
$\equiv FeOH + Mg^{2+} + H_2PO_4^- \leftrightarrow \equiv FeOMgHPO_4^- + 2H^+$	−4.75
$\equiv FeOH + Mg^{2+} + H_2PO_4^- \leftrightarrow \equiv FeOMgH_2PO_4^0 + H^+$	3.11
$\equiv FeOH + Ca^{2+} + H_2PO_4^- \leftrightarrow \equiv FeOCaHPO_4^- + 2H^+$	−6.44
$\equiv FeOH + Ca^{2+} + H_2PO_4^- \leftrightarrow \equiv FeOCaH_2PO_4^0 + H^+$	0.19

All stability constants are intrinsic constants (modified from Gao and Mucci, 2001).

$$\begin{aligned} \text{Stotal} = {} & [\equiv FeOH] + [\equiv FeO^-] + [\equiv FeOH_2^+] \\ & + [\equiv FePO_4^{2-}] + [\equiv FePO_4H^-] + [\equiv FePO_4H_2] \\ & + [\equiv FeOMg^+] + [\equiv FeOCa^+] \\ & + [\equiv FeOMgHPO_4^-] + [\equiv FeOMgH_2PO_4^0] \\ & + [\equiv FeOCaHPO_4^-] + [\equiv FeOCaH_2PO_4^0] \end{aligned} \quad (2)$$

where [] denotes concentrations, and ≡ represents the mineral surface lattice. The model is closed mathematically by specifying values for the independent variables; H^+ (pH), and the concentrations of (free) dissolved Na^+, Mg^{2+} and Ca^{2+}, plus Stotal and Ptotal. To account for non-specific, or electrostatic, interactions at the mineral surface (Morel and Hering, 1993), the ionic strength of the solution, I, is also specified.

More than 50% of DIP in seawater is complexed with the major cations Na^+, Mg^{2+} and Ca^{2+} (Atlas et al., 1976). We consider the formation of the three Na-phosphate aqueous complexes ($NaH_2PO_4^0$, $NaHPO_4^-$ and $NaPO_4^{2-}$; Gao and Mucci, 2001) and the three dominant Mg- or Ca-phosphate complexes in seawater ($MgHPO_4^0$, $CaHPO_4^0$ and $CaPO_4^-$) (Eq. 1), but neglect Mg- and Ca-phosphate aqueous complexes that contribute less than 2% of the total aqueous DIP concentration. We also neglect the adsorption of anions other than phosphate (e.g., sulfate), because their competitive effects are only significant at relatively low pH values, which fall outside the pH range of interest in the present study (Geelhoed et al., 1997; Gao and Mucci, 2003). The results of Gao and Mucci (2003) further indicate that the formation of Mg^{2+}, Ca^{2+}, and ternary cation–phosphate surface complexes (≡FeO-Mg^+, ≡$FeOCa^+$, ≡$FeOMgHPO_4^-$, ≡$FeOMgH_2PO_4^0$, ≡$FeOCaHPO_4^-$ and ≡$FeOCaH_2PO_4^0$) (Eq. 2) affect phosphate sorption to goethite in artificial seawater solutions.

2.2. Independent variables and forcing functions

2.2.1. Stotal and ptotal

When the model is applied to the laboratory experiments of Gao and Mucci (2001, 2003), the Ptotal and Stotal values reported by these authors are imposed (Section 3). When calculating the speciation along pH-salinity gradients, Ptotal is assigned values between 1 and 10 μM, while Stotal is varied between 5 and 20 μM. Within these ranges of Ptotal and Stotal, the model predicts DIP concentrations on the order of 1–5 μM, which is typical for both surface (e.g., Van der Zee et al., 2007) and subterranean estuaries (Charette et al., 2005). Further details are given in Section 4.

2.2.2. Ionic strength and major ion aqueous composition

The activity coefficients (γ) of aqueous species are calculated using the same form of the Davies equation as in Gao and Mucci (2001):

$$\log \gamma = -0.5z^2\left(\frac{\sqrt{I}}{1+\sqrt{I}}\right) - 0.2I \quad (3)$$

where I is the ionic strength of the solution (M) and z is the charge of the ion. All calculations are performed at a temperature of 25 °C and total pressure of 1 bar. Activity corrections are included in the equilibrium calculations, in which either a fixed ionic strength (Section 3) or a linear mixing gradient (Section 4) along the estuarine transect from freshwater ($I = 0.001$ M; $S = 0.05$) to seawater ($I = 0.7$ M; $S = 35$) is considered. The major cation composition of the water is obtained by linear interpolation between the concentrations in seawater (Na^+: 466.95 mM; Mg^{2+}: 52.82 mM; Ca^{2+}: 10.28 mM) and those in freshwater (Na^+: 0.1 mM; Mg^{2+}: 0.04 mM; Ca^{2+}: 0.2 mM).

2.2.3. Surface charging

An electric potential, Ψ_0 (volts), develops on the surface of goethite as a result of the formation of charged surface species. The surface charge density σ (C m^{-2}) is given by (e.g., Stumm, 1992):

$$\sigma = \frac{F}{SSA \cdot C_s} \cdot \Gamma \quad (4)$$

where F is Faraday's constant (C mol^{-1}), SSA is the specific surface area of goethite (m^2 g^{-1}), C_s is the mass of sorbent in contact with a liter of solution (g dm^{-3}) and Γ is the net volumetric concentration of surface charge (M):

$$\begin{aligned} \Gamma = {} & [\equiv FeOH_2^+] + [\equiv FeOMg^+] + [\equiv FeOCa^+] \\ & - [\equiv FeO^-] - [\equiv FePO_4H^-] - 2[\equiv FePO_4^{2-}] \\ & - [\equiv FeOMgHPO_4^-] - [\equiv FeOCaHPO_4^-] \end{aligned} \quad (5)$$

In the CCM, σ and Ψ_0 are linearly related through the capacitance, C (farad m^{-2}):

$$C = \frac{\sigma}{\psi_0} \tag{6}$$

The CCM was originally developed for high ionic strength conditions (Schindler and Stumm, 1987), where a linear decrease in potential with distance from the surface is assumed, as opposed to low ionic strength conditions, in which the charge distribution typically behaves like an electrical double layer. The application of the CCM can be extended to variable ionic strength, provided that the effect of I is accounted for in the value of C. According to Lützenkirchen (1999):

$$C = \varepsilon_r \varepsilon_0 \kappa = 2.28\sqrt{I} \tag{7}$$

where ε_r is the relative dielectric constant of water (dimensionless), ε_0 is the permittivity of vacuum (farad m^{-1}) and κ is the inverse Debye length (m^{-1}).

The effect of surface charging is included in the equilibrium calculations by correcting the intrinsic formation constants of charged surface species for non-specific (electrostatic) interactions. For example, for the surface complexation reaction

$$\equiv \mathrm{FeOH} + \mathrm{H_2PO_4^-} \leftrightarrow \equiv \mathrm{FePO_4H^-} + \mathrm{H_2O} \tag{8}$$

the apparent formation constant is:

$$K'_{app} = \frac{K_{int} \cdot \gamma_{\mathrm{H_2PO_4^-}}}{SP} \tag{9}$$

where K_{int} refers to the intrinsic stability constant, and SP, the surface potential term, is defined as (Morel and Hering, 1993):

$$SP = \exp\left(\frac{-\Delta z F \Psi_0}{RT}\right) \tag{10}$$

In the example above, Δz, the net change in charge associated with the formation of the surface species, is equal to -1. R is the gas constant (J mol^{-1} K^{-1}) and T is temperature (K).

Since the speciation is a function of Ψ_0 through the SP term, whereas Ψ_0 is itself a function of σ (and thus of the speciation), finding the values of Ψ_0, σ and the speciation for any possible combination of pH, ionic strength, solution composition, Stotal and Ptotal requires an iterative procedure. The iterative solution is implemented numerically using the bisection method (Press et al., 1992).

2.2.4. pH

The pH (NBS scale) is treated as an independent variable in the SCM calculations. In the simulations performed at fixed ionic strength (Section 3), the value of pH is varied linearly from 4 to 10 using discrete unit intervals. In the equilibrium calculations performed along the mixing gradients of freshwater and seawater (Section 4), the pH distributions are assumed to result from the conservative mixing between fresh and seawater end-members of given alkalinity (Alk) and dissolved inorganic carbon (DIC). The hypothesis of conservative mixing is obviously a simplifying assumption, especially in surface estuaries where the carbonate system is influenced by biogeochemical processes and by gas exchange with the atmosphere (e.g., Regnier et al., 1997; Vanderborght et al., 2002). Note that, even under the conservative mixing assumption for Alk and DIC, pH itself is a non-linear function of salinity. The concentration of DIC ($CO_2(aq) + H_2CO_3 + HCO_3^- + CO_3^{2-}$), as well as the distribution of carbonate species are calculated from the specified pH and carbonate alkalinity (Alk_C) of the two end-member solutions (Table 4). Further details on the calculation of Alk and DIC are given in the Appendix.

The imposed end-member pH values for the surface estuary are 7.5 (freshwater) and 8.2 (seawater), and 5.7 (freshwater) and 8.2 (seawater) for the subterranean estuary. The river end-member values selected for pH and Alk (Table 4) in the surface estuary simulations are typical of those measured in heterotrophic estuaries, such as the Loire (Abril et al., 2003) or the Scheldt (Hellings et al., 2001; Vanderborght et al., 2002). Lower river end-member pH values have been reported, e.g., for estuaries of the Southeastern U.S. (Cai and Wang, 1998) and estuaries impacted by acid mine drainage (Elbaz-Poulichet et al., 1999), while higher values have been observed in river systems dominated by net autotrophy (Howland et al., 2000; De la Paz et al., 2007). The relatively high river Alk value falls within the range reported for the Guadalquivir (De la Paz et al., 2007) and Mississippi estuaries (Cai, 2003), which are under the influence of river water draining carbonate-rich basins. In these systems, the buffering capacity is significant and Alk decreases monotonously with increasing salinity, until seawater values are reached. A reverse trend is sometimes observed in estuaries characterized by river water Alk concentration lower than seawater (e.g. Devol et al., 1987; Cai and Wang, 1998; Brasse et al., 2002; Zhai et al., 2007).

The computed pH profiles along the salinity gradients in the surface and subterranean estuaries are shown in Fig. 1. The pH profile in the surface estuary shows an initial decrease, reaching a minimum around a salinity of 3.5 (see also Mook and Koene, 1975). A persistent minimum in pH at low salinities has been observed in field studies of the Rhine, Scheldt, Fraser and Tamar estuaries (Howland et al., 2000). At salinities higher than 10, pH increases roughly linearly with salinity, up to 8.2. In the subterranean estuary, the pH versus salinity distribution exhibits a pronounced change in slope at salinity around 25. This pH distribution roughly follows the trend observed along a beach transect in the subterranean estuary of Waquoit Bay, MA (Spiteri et al., 2006).

Table 4
Chemical composition of freshwater and seawater end members in the model surface and subterranean estuaries

	Riverwater (surface estuary)	Groundwater (subterranean estuary)	Seawater (surface and subterranean estuary)
pH	7.5	5.7	8.2
Alkalinity (mM)	4.97	0.6	2.487
Salinity (‰)	0.05	0.05	35
Ionic strength (M)	0.001	0.001	0.7

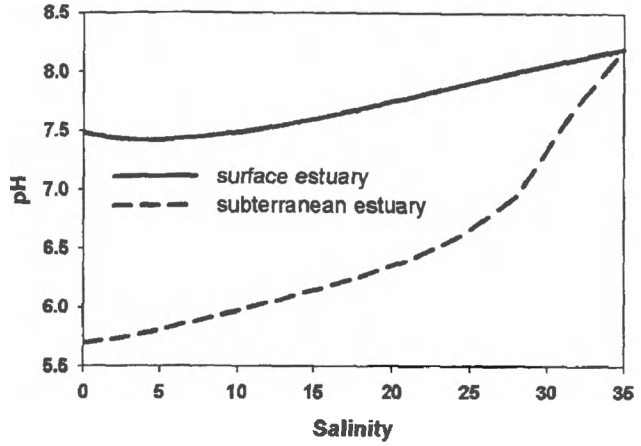

Fig. 1. Computed pH distributions in the model surface and subterranean estuaries. (See text for complete discussion).

In summary, the speciation calculations are based on the following assumptions.

1. Alk and DIC behave conservatively during mixing of fresh groundwater and seawater, resulting in a non-linear pH distribution between the two end-member pH values as a function of salinity (Fig. 1).
2. The major ions mix conservatively, thereby allowing us to calculate I for each mixing ratio. The effect of ionic strength on the aqueous speciation is included by computing aqueous activity coefficients with Davies' equation (Eq. 3).
3. The mineral surface charge is derived from the CCM, in which σ varies linearly with Ψ_0. Given the large salinity range considered, the effect of variable ionic strength on the value of capacitance is accounted for by Eq. (7). The effect of surface charging is included in the calculation of the apparent formation constants of charged surface complexes through the surface potential term, SP (Eq. 9).
4. For a given solution composition, the values of σ and SP are computed iteratively from the specified pH, major cation solution composition, ionic strength, Ptotal and Stotal.

3. PHOSPHATE ADSORPTION: PH AND IONIC STRENGTH EFFECTS

Comparison of model results with observations is performed in two steps. First, using the reaction network and intrinsic stability constants given in Table 2, we compare predicted and measured phosphate adsorption isotherms to goethite in 0.7 M NaCl solution, using the experimental data of Gao and Mucci (2001). Second, the aqueous and surface complexes involving $Ca^{2+}$and Mg^{2+} (Table 3) are included in the SCM, and the model isotherm is compared to the experimental data obtained in artificial seawater solution by Gao and Mucci (2003). Then, having established that the set of intrinsic stability constants in Tables 2 and 3 is able to reproduce the high ionic strength data, the model is used to contrast pH-dependent phosphate adsorption under seawater and freshwater conditions.

3.1. Speciation in NaCl solutions (0.001 and 0.7 M)

The model-predicted dependence of phosphate adsorption on pH in 0.7 M NaCl solution gives a good match (within ±10%) to the observed trend of phosphate binding to goethite over pH range 4–10 (Fig. 2). Also shown are the isotherms calculated when increasing or decreasing the total site density, Stotal, by 10% relative to the value reported by Gao and Mucci (2001). Phosphate adsorption is predicted to be relatively constant between pH 4 and 7, and to decrease at higher pH. The sensitivity to Stotal also decreases with increasing pH when pH >7.

The modeled pH-dependent adsorption isotherms in high (0.7 M) and low (0.001 M) ionic strength NaCl solutions are compared in Fig. 3a. In pH range 5–10, phosphate adsorption is higher in 0.7 M than in 0.001 M NaCl solution. The two adsorption isotherms cross over at pH 5 and an opposite trend is observed for pH < 5. The general shape of the adsorption isotherm remains the same when Stotal is varied by ±10%. Enhanced adsorption on goethite at low ionic strength under acidic conditions agrees with the experimental observations of Barrow et al. (1980) and the model results of Hiemstra and Van Riemsdijk (1996). The same trend was also observed by Antelo et al. (2005), who investigated the adsorption of phosphate onto goethite in 0.1 and 0.01 M KNO_3. In the latter study, however, the cross over point occurred at a somewhat lower pH (~4).

To better understand the combined effects of ionic strength and pH on phosphate adsorption, two pH values (4 and 9) with contrasting speciation are considered. The dominant solute and surface species at pH 4, as determined by solution pH and composition, are $H_2PO_4^-$, $\equiv FeOH_2^+$ and $\equiv FePO_4H_2^0$. Sorption is therefore mainly controlled by the following equilibrium:

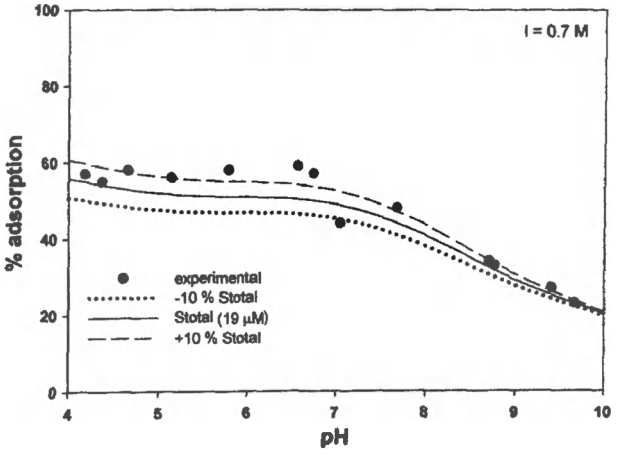

Fig. 2. Phosphate adsorption to goethite as a function of pH in 0.7 M NaCl solution. The total phosphate concentration (Ptotal) equals 24 µM, the total surface site concentration (Stotal) is 19 µM. The solid line is the model-predicted adsorption isotherm. Also shown are the predicted adsorption isotherms for a 10% increase or 10% decrease in Stotal. The experimental data points, and the values of Ptotal and Stotal, are taken from Gao and Mucci (2001). The constant capacitance C calculated with Eq. 7 is 1.92 F m^{-2}.

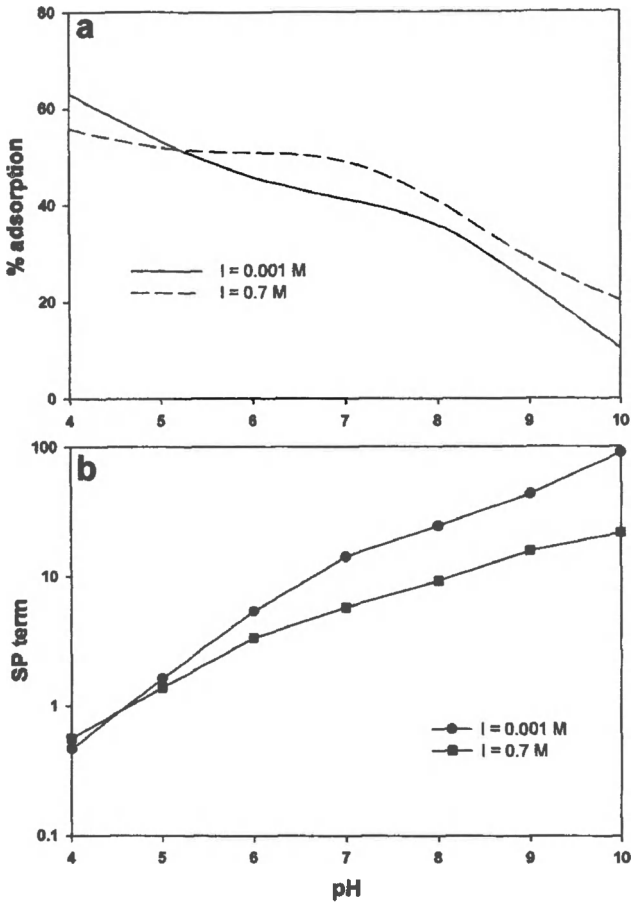

Fig. 3. Comparison of model-predicted (a) adsorption isotherms, and (b) surface potential terms (SP, Eq. 10) for phosphate adsorption to goethite in low (0.001 M) and high (0.7 M) ionic strength NaCl solutions. Note that the adsorption isotherm for $I = 0.7$ M in panel (a) is identical to the solid curve in Fig. 2.

$$\equiv FeOH_2^+ + H_2PO_4^- \leftrightarrow \equiv FePO_4H_2^0 + H_2O \quad (11)$$

with

$$[\equiv FeH_2PO_4^0] = K_{sc_1} \cdot \frac{[\equiv FeOH_2^+] \cdot [H_2PO_4^-] \cdot \gamma_{H_2PO_4^-}}{SP} \quad (12)$$

where [] denotes concentrations, and K_{sc_1} is the intrinsic stability constant. Eq. (12) shows that non-specific interactions at the mineral surface (via SP) and in solution (via $\gamma_{H_2PO_4^-}$) influence the extent of phosphate adsorption. At low ionic strength, $\gamma_{H_2PO_4^-}$ approaches 1, resulting in a higher concentration of adsorbed phosphate under the form of $[\equiv FeH_2PO_4^0]$, as compared to the high ionic strength solution in which $\gamma_{H_2PO_4^-}$ is significantly lower than 1. At pH 4, the value of SP is less than 1 (Fig. 3b), with a slightly lower value at low (SP = 0.46) compared to high ionic strength (SP = 0.56), contributing further to the increased adsorption of phosphate at low ionic strength and low pH (Fig. 3a; Eq. 12).

At pH 9, the dominant species are HPO_4^{2-}, ≡FeOH and $\equiv FePO_4^{2-}$. Hence, the following equilibrium controls phosphate adsorption at high pH:

$$\equiv FeOH + HPO_4^{2-} \leftrightarrow \equiv FePO_4^{2-} + H_2O \quad (13)$$

such that

$$[\equiv FePO_4^{2-}] = \frac{K_{sc_2} \cdot [\equiv FeOH] \cdot [HPO_4^{2-}] \cdot \gamma_{HPO_4^{2-}}}{SP^2} \quad (14)$$

where K_{sc2} is the intrinsic stability constant, and the second order dependence on SP results from the divalent charge of the surface complex, $\equiv FePO_4^{2-}$. The increasing divergence of the surface electrical potential at low and high ionic strength as the solution becomes more alkaline (Fig. 3b) helps explain the reversal in the ionic strength dependence of phosphate adsorption (Fig. 3a). At pH 9, the value of SP at low ionic strength (~42) is significantly higher than that at high ionic strength (~16), thereby lowering $[\equiv FePO_4^{2-}]$. Although at pH 9 the effect of $\gamma_{H_2PO_4^-}$ acts in the opposite way ($\gamma_{H_2PO_4^-} = 0.87$ and 0.23 at I = 0.001 and 0.7 M, respectively), the inverse dependence of the extent of adsorption on SP^2outweighs that of $\gamma_{H_2PO_4^-}$. Note that the dependencies of SP on ionic strength and pH illustrated in Fig. 3b agree qualitatively with the trends reported by Dzombak and Morel (1990) for phosphate adsorption to hydrous ferric oxide.

The relative effects on phosphate adsorption of the electrical charging of the goethite surface, the non-specific electrostatic interactions in solution, and the formation of aqueous complexes are further illustrated in Fig. 4 for the 0.7 M NaCl solution. As expected, when the aqueous complexes are ignored ("no aqueous complexes"), phosphate adsorption is predicted to increase (Fig. 4a), as more free phosphate, which would otherwise bind to Na^+, is available for adsorption. In addition, the effect becomes more pronounced at higher pH values, because the concentration of Na-phosphate aqueous complexes increases with pH (Fig. 4b). When non-specific interactions in solution are also ignored, phosphate adsorption increases even further, because all dissolved phosphate is now assumed to exist as free ions ($\gamma = 1$). Phosphate adsorption at pH >7 is particularly sensitive to γ values. Finally, when the electric potential Ψ_0 at the goethite surface is set to 0 (SP = 1), phosphate adsorption is greatly overestimated, especially at high pH. As shown in Fig. 3b, the surface electrostatic effects become more pronounced because of the enhanced importance of repulsion with increasing pH.

The results of the sensitivity analysis highlight the important role of electrostatic interactions, in solution and at the mineral–solution interface, on phosphate adsorption onto iron (hydr)oxides. Hence, models that do not account for these interactions (e.g., K_d-models or non-electrostatic SCMs) are not appropriate to reproduce the adsorption behavior of phosphate to these mineral phases under the highly variable salinity and pH conditions encountered in estuaries and coastal aquifers.

3.2. Speciation in artificial freshwater and seawater solutions

The reaction network of Tables 2 and 3 is applied to phosphate adsorption from artificial freshwater and seawater solutions containing Mg^{2+} and Ca^{2+} cations, in addition to Na^+. The model-predicted isotherm in artificial seawater ($I = 0.7$ M; 466.95 mM Na^+, 52.82 mM Mg^{2+} and 10.28 mM Ca^{2+}) compares favorable to the experimental

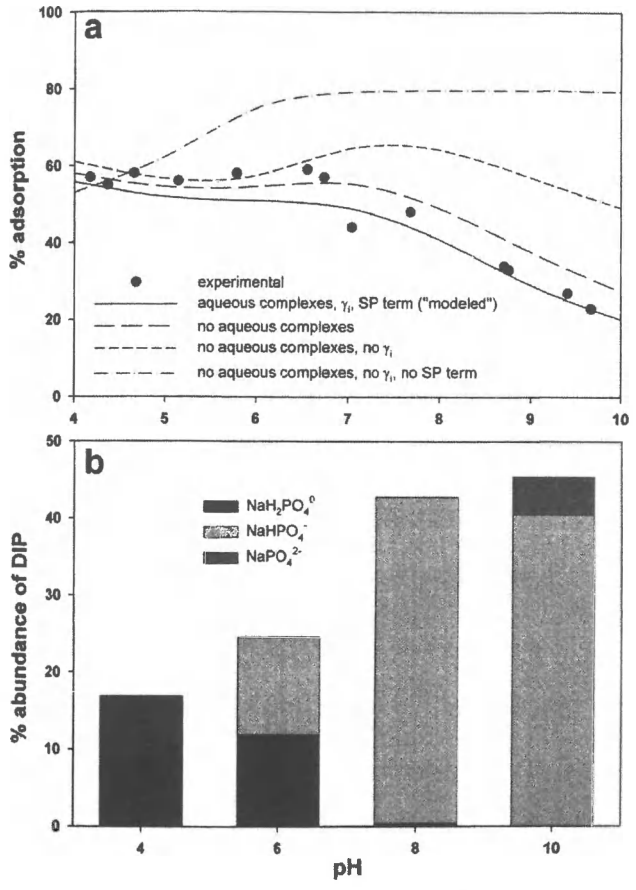

Fig. 4. (a) Model-predicted effects of ignoring the formation of aqueous complexes, aqueous activity corrections (γ) and electrostatic interactions at the mineral–solution interface (SP term) on phosphate adsorption to goethite in 0.7 M NaCl solution, using the simplified reaction network in Table 2. The experimental data points, and the values of Ptotal and Stotal are from Gao and Mucci (2001). The solid line is identical to the dashed line in Fig. 3a. (b) Relative abundance of the three Na-phosphate complexes for different values of pH. Ptotal is equal to 24 μM and Stotal is 19 μM.

data of Gao and Mucci (2003) in Fig. 5a, which fall well within the assigned ±10% uncertainty to Stotal. Although the data set is more limited than that for the 0.7 M NaCl solution, the experimental results indicate that for pH < 6 adsorption is higher in artificial seawater than in NaCl solution (compare Figs. 2 and 5). In pH range 7–8.5, however, phosphate adsorption is very similar in both solutions. The model-predicted adsorption isotherm underestimates the extent of phosphate adsorption at pH <6.0, while pH >6.5 sorption is overestimated.

The adsorption isotherm calculated for the artificial freshwater solution ($I = 0.001$ M; Na^+: 0.1 mM; Mg^{2+}: 0.04 mM; Ca^{2+}: 0.2 mM) exhibits two "cross-over" points with that for artificial seawater (Fig. 5b). For most of the pH range of interest (5.7–8.2), both the NaCl (Table 2) and extended reaction networks (Tables 2 and 3) predict increased sorption at the higher ionic strength.

Comparison of the modeled aqueous and surface speciation for typical freshwater and seawater conditions clearly illustrates the need to account for the interactions of phosphate with the major seawater cations during estuarine mixing (Fig. 6). In freshwater, inorganic aqueous phosphate speciation at pH 5.5 is dominated by $H_2PO_4^-$. In seawater of pH 8.0, the aqueous speciation is far more diverse. The largest fraction of aqueous phosphate is composed of $MgHPO_4^0$ (48%), followed by HPO_4^{2-} (28%) and $NaHPO_4^-$ (14%) (see also Atlas et al., 1976). The two ternary Mg-phosphate surface complexes ($\equiv FeoMgHPO_4^{2-}$ and $\equiv FeOMgH_2PO_4^0$) make up ~90% of total adsorbed phosphate in seawater, while in freshwater the speciation is dominated by $\equiv FeHPO_4^-$ and $\equiv FeH_2PO_4^0$ (Fig. 6). The formation of the ternary surface complexes compensates for the desorption triggered by an increase in ionic strength upon estuarine mixing. The effect of ternary complexes is in line with the results of Gao and Mucci (2003), who show that when the ternary complexes are ignored phosphate desorption in seawater is overestimated.

4. PHOSPHATE ADSORPTION IN ESTUARIES

The reaction network of Tables 2 and 3 is used to simulate phosphate adsorption to goethite along physico-chemical gradients of ionic strength and pH typical of surface estuaries and coastal aquifers. For each salinity value that is used as the mixing index of freshwater and seawater, the corresponding ionic strength and the concentration of the three major cations (Na^+, Ca^{2+} and Mg^{2+}) are determined, assuming that the major ions behave conservatively upon estuarine mixing. For a given solution composition, a value of SP is computed based on the pH, solution composition, ionic strength, Ptotal and Stotal. The SCM is applied to the nonlinear pH mixing curves of the model surface and subterranean estuaries presented in Fig. 1.

4.1. Baseline simulations

The roles of pH and ionic strength in phosphate adsorption are assessed for Ptotal equal to 10 μM and Stotal ranging from 5 to 20 μM. In the surface estuary (Fig. 7a), for any given value of Stotal, phosphate adsorption increases from the freshwater end-member to ~1 salinity, while further increase in salinity up to 35 causes a progressive desorption. Phosphate adsorption in the subterranean estuary (Fig. 7b) exhibits a significantly different dependence on salinity. Adsorption increases slowly from the freshwater end-member to 25 salinity, followed by a sudden desorption under more saline conditions. The distinct salinity dependencies of phosphate adsorption in the surface and subsurface estuaries seen in Fig. 7 reflect the different pH-salinity relationships in the two environments (Fig. 1), together with the influence of ionic strength on adsorption. In both cases, the SCM calculations predict non-conservative behavior of dissolved phosphate during freshwater–seawater mixing.

4.2. Surface estuary: the Scheldt

In a recent study, Van der Zee et al. (2007) measured longitudinal profiles of dissolved and particulate phosphate along the salinity gradient of the Scheldt estuary, a well-mixed coastal plain estuary in NW Europe. According to

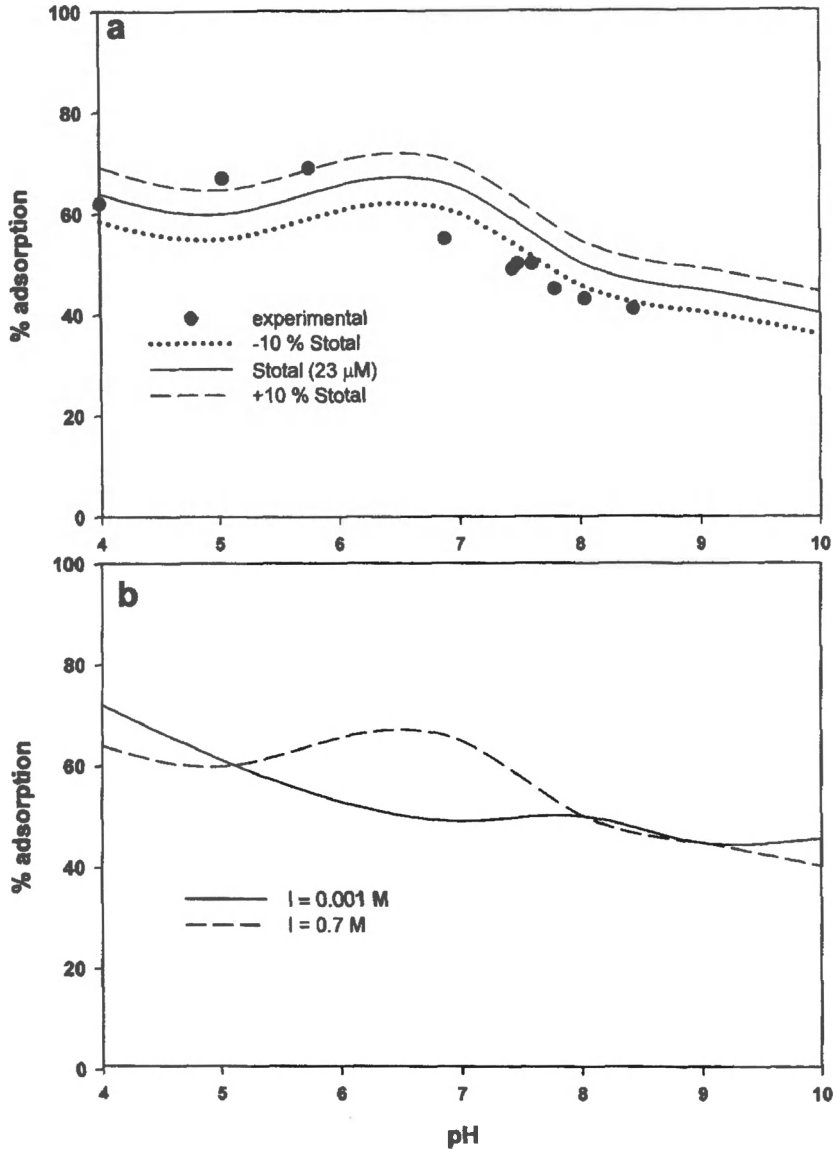

Fig. 5. (a) Phosphate adsorption to goethite as a function of pH in artificial seawater solution. The total phosphate concentration (Ptotal) equals 24.9 μM, the total surface site concentration (Stotal) is 23 μM. The solid line is the model-predicted adsorption isotherm, using the extended reaction network of Tables 2 and 3. Also shown are the predicted adsorption isotherms for a 10% increase or 10% decrease in Stotal. The experimental data points and the values of Ptotal and Stotal are from Gao and Mucci (2003). (b) Comparison of modeled phosphate adsorption isotherms in artificial freshwater ($I = 0.001$ M; Na^+: 0.1 mM; Mg^{2+}: 0.04 mM; Ca^{2+}: 0.2 mM) and artificial seawater ($I = 0.7$ M; Na^+: 466.95 mM; Mg^{2+}: 52.82 mM; Ca^{2+}:10.28 mM) ionic strength solutions.

these authors, the main process affecting phosphorus dynamics in the Scheldt estuary is desorption of inorganic phosphate from suspended particulate matter (SPM) with increasing salinity. The most likely sorbents of phosphate are authigenic ferric iron precipitates actively forming in the upper estuary (Wollast, 1982; Hyacinthe and Van Cappellen, 2004).

The formation of turbidity maxima is a typical feature in numerous estuaries (e.g., Festa and Hansen, 1976; Uncles and Stephens, 1993). In the Scheldt, a pronounced turbidity maximum develops at low salinities (Wollast, 1988). As a result, concentrations of SPM drop from 100 to 200 mg L^{-1} in the upper estuary (0–5) to 50–100 mg L^{-1} in the lower estuary (10–30) (Fig. 8a). Both measurements and hydrodynamic modeling indicate that the SPM distribution, which results from the combined effects of transport and exchange with the estuarine bed, can be approximated by an exponentially decreasing function with respect to salinity (Arndt et al., 2007). In the calculations below, we compare the exponential SPM distribution to constant and linear SPM distributions (Fig. 8a).

In the Scheldt estuary, the very high river end-member DIC concentrations (Table 4), together with the similar magnitudes of CO_2 outgassing and organic matter decomposition (Vanderborght et al., 2002), lead to a roughly linear distribution of DIC versus salinity. Nitrification is the main process responsible for the departure from conservative behavior of alkalinity, thereby reinforcing the pH drop due to mixing in the low salinity region (Vanderborght et al., 2002). However, the influence of nitrification in the upper estuary has decreased significantly over the last decade (Vanderborght et al., 2007). The hypothesis of conservative mixing of Alk is therefore a reasonable first-order approximation to estimate pH values.

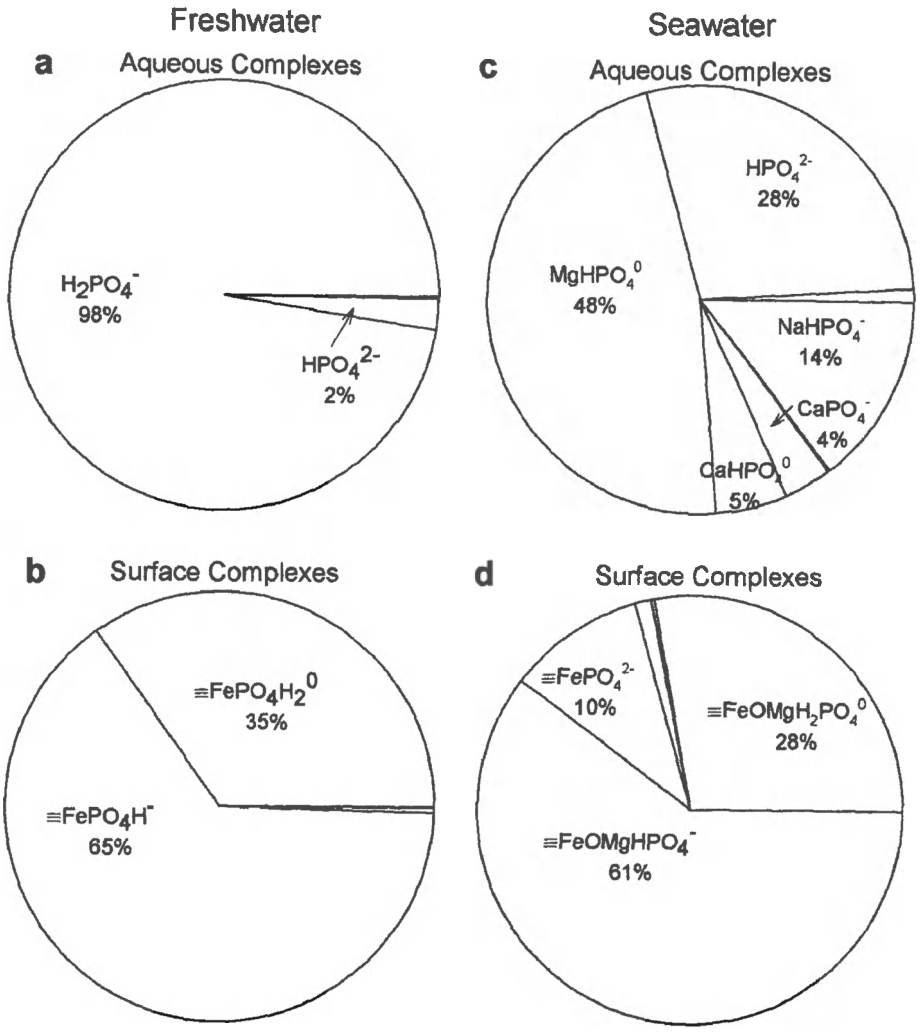

Fig. 6. Modeled aqueous and surface speciation of phosphate in freshwater (pH 5.5; Na^+: 0.1 mM; Mg^{2+}: 0.04 mM; Ca^{2+}: 0.2 mM) and seawater (pH 8.0; Na^+: 466.95 mM; Mg^{2+}: 52.82 mM; Ca^{2+}:10.28 mM). The calculations assume goethite is the only solid phase binding phosphate.

To apply the SCM to the Scheldt estuary, we assume that the measured concentrations of particulate inorganic phosphate (PIP) represent the pool of phosphate that can be desorbed from SPM (i.e., PIP = SIP). Note that PIP is assumed to be fully desorbable whereas in reality it can also occur as detrital mineral grains or be occluded in clays and/or metal oxides. The field measurements of Van der Zee et al. (2007) further show that total inorganic phosphate (Ptotal = DIP + SIP) behaves conservatively along the salinity gradient and can, thus, be represented by a linear distribution with respect to salinity. Based on the available data, the freshwater and seawater end-members are assigned Ptotal concentrations of 10 and 1 μM, respectively. The distribution of the total number of adsorption sites (Stotal) is estimated from the imposed SPM distributions (Fig. 8a), assuming that the Fe content of SPM decreases linearly from 5% to 3% between the freshwater and seawater end-members (Zwolsman, 1994), and that ~10% of the iron is available for phosphate adsorption (Slomp et al., 1996).

Figs. 8c and d show the measured dissolved and particulate inorganic phosphate distributions in the water column of the Scheldt estuary, respectively. The modeled distributions, computed without any adjustments of the parameter values in the SCM, are also plotted for the different hypothetical SPM distributions. In the case of the exponential SPM distribution, both model and field results imply a release of DIP from particulate matter in the salinity range 5–12. For the two other SPM distributions, the model-calculated DIP profiles differ considerably from the observed ones. In particular, they predict a net removal of DIP by adsorption in the low salinity region of the estuary, because the decrease in Ptotal is larger than that of Stotal (Ptotal/Stotal <1; Fig. 8b). Thus, as expected, the imposed SPM distribution is essential to reproduce the observed inorganic phosphate distributions in the estuary using the SCM model (see also Fig. 7a).

According to the model calculations, the release of DIP at mid-salinities is mainly due to the rapid drop in SPM, and hence Stotal, downstream of the turbidity maximum, which gives rise to Ptotal/Stotal ratios significantly higher than 1.0 (Fig. 8b). Note, however, that the maxima in Ptotal/Stotal and DIP do not coincide, because phosphate adsorption also depends on the variable salinity and pH conditions encountered along the estuarine gradient. In fact, the SCM predicts that the formation of ternary Mg-phosphate surface complexes upon admixing of seawater

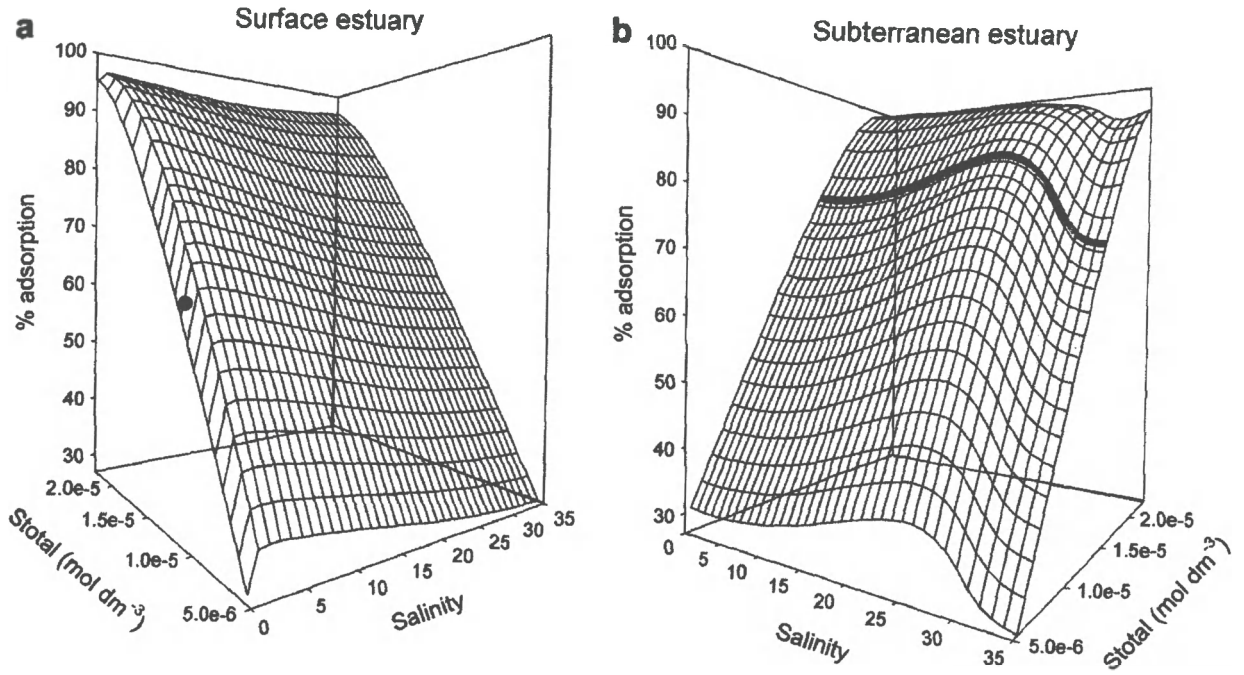

Fig. 7. Phosphate adsorption to goethite in the model (a) surface and (b) subterranean estuaries, computed as a function of salinity and the total concentration of surface sites (Stotal range: 5–25 μM). The total (dissolved plus adsorbed) phosphate concentration is kept constant at 10 μM. The black dot in panel (a) corresponds to the freshwater boundary conditions in the surface estuary application (Section 4.2). The thick line in panel (b) corresponds to the Stotal value imposed in the subterranean estuary application (Section 4.3).

limits the extent of desorption caused by the exponential decrease of Stotal with increasing salinity. This is why the peak value of the DIP concentration occurs at a slightly lower salinity than that of Ptotal/Stotal.

The abundance of reactive iron mineral phases in the SPM of the Scheldt estuary, and the relatively minor role of phosphate transformation processes other than sorption (such as limited biological uptake in the brackish part of the Scheldt estuary; Van der Zee et al., 2007), explain why the simple SCM reproduces the general trends of the DIP and SIP distributions in this particular estuary. In turn, the model results point to the need to characterize in more detail the nature and surface properties of phosphate sorbents along estuarine gradients, and to critically re-assess previously proposed mechanisms of phosphate desorption during freshwater–seawater mixing. In particular, the results suggest that the increasing concentrations of major seawater cations, with which phosphate can form aqueous complexes, may not in themselves cause the release of phosphate from SPM during mixing.

4.3. Subterranean estuary: phosphate dynamics during seawater intrusion

The SCM is coupled to a two-dimensional (2D) density-dependent, finite-element groundwater flow model (RT-FEM, Meile and Tuncay, 2003) to simulate the transient response of phosphate adsorption following saltwater intrusion in a coastal aquifer. The flow model and its application to reactive transport in coastal environments is described in detail elsewhere (Spiteri et al., 2008). The effect of groundwater salinization is simulated in a confined aquifer of 20 m × 10 m size. The model setup is based on the standard benchmark Henry problem of seawater intrusion (e.g., Simpson and Clement, 2003). With a permeability of 1×10^{-9} m^{2}and a landward freshwater head of 0.27 m, the average landward recharge rate is 6.6×10^{-5} ms^{-1}, equivalent to that specified in the Henry problem. The initial conditions before salt penetration assume homogeneous distributions of salinity (0.05), pH (5.7), DIP (2 μM), Ptotal (10 μM) and Stotal (15 μM). Note that the imposed DIP concentration corresponds to the equilibrium value with respect to adsorption onto goethite (Fig. 7b).

Two transient simulations are performed. In the first scenario, the DIP concentration of the intruding seawater is equal to the freshwater value (2 μM). In a second scenario, the concentration of DIP in the intruding seawater is assumed to be half that of freshwater (1 μM). In what follows, the two scenarios are referred to as "without dilution" and "with dilution".

The propagation of salt shows the classic pattern of the Henry problem. This is illustrated in Fig. 9a for the groundwater salinity recorded at mid-depth (5 m) within the coastal aquifer. The corresponding, time-dependent, longitudinal concentration profiles of DIP and SIP are plotted in Fig. 9b–e. In both scenarios, an initial adsorption of DIP contained in the inflowing seawater occurs at the seaward boundary (profile at $t = 125$ min), followed rapidly by desorption ($t = 500$ min and later) and the subsequent landward propagation of the DIP pulse at the leading edge of the intruding seawater (Figs. 9b and d). The desorption of phosphate is mainly due to the rapidly rising pH when salinity increases above 25 (Fig. 1). With time, the DIP peak progressively disappears until, at steady-state, the concentration returns to the constant value of 2 μM in the scenario without dilution (Fig. 9b), and follows a conservative mixing curve in the scenario with dilu-

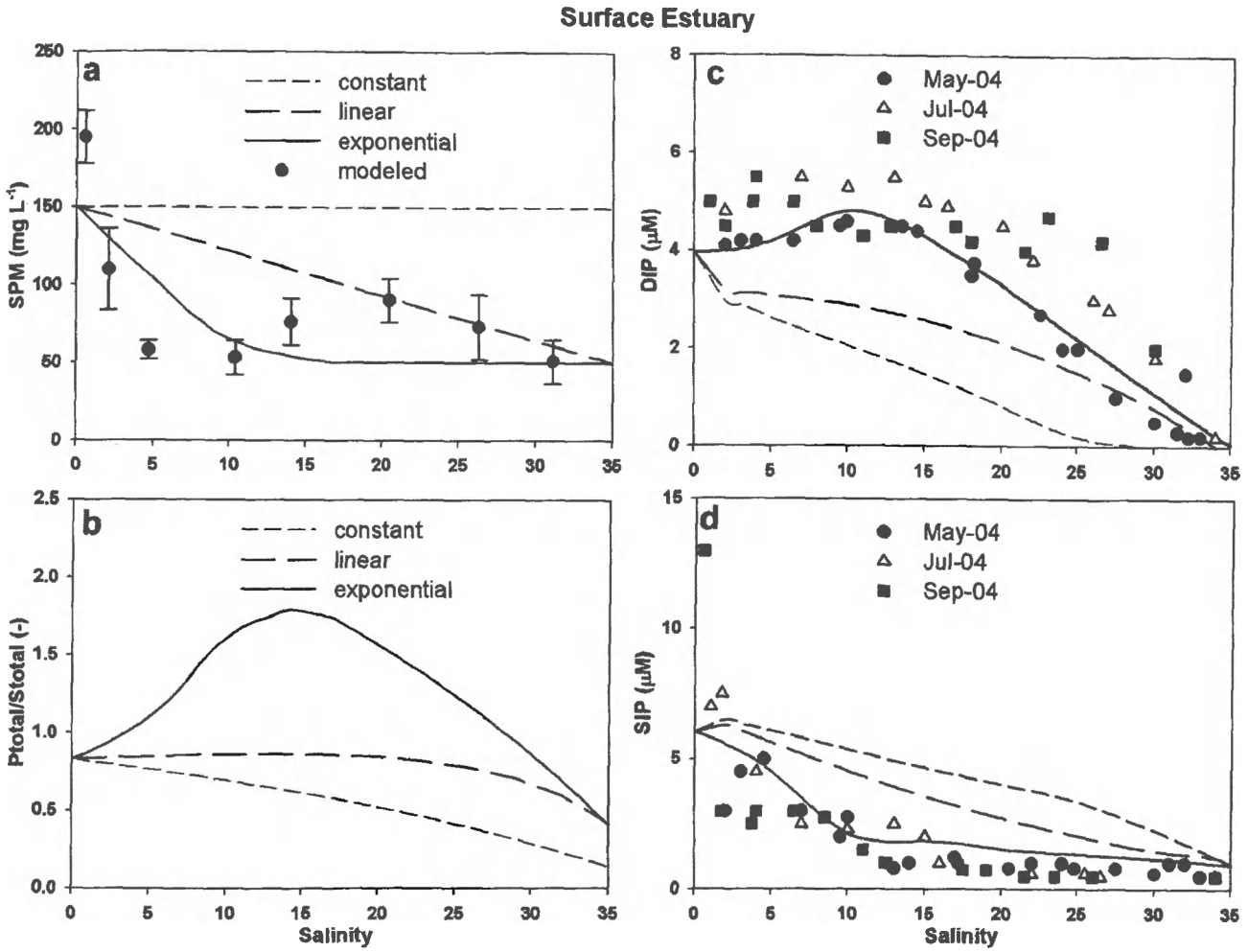

Fig. 8. Distributions of (a) the suspended particulate material (SPM) concentration, (b) the molar ratio of total (dissolved plus adsorbed) phosphate to total surface binding site (Stotal) concentrations, (c) the dissolved phosphate concentration and (d) the adsorbed phosphate concentration in the water column of the Scheldt estuary, plotted against salinity. The symbols in (c) and (d) correspond to measurements for three different sampling times in 2004 (Data source: Van der Zee et al., 2007). The DIP and SIP are equivalent to the soluble reactive phosphorus (PO_4) and particulate inorganic phosphorus (PIP) concentrations reported by Van der Zee et al. (2007). Note also that the imposed 10 µM freshwater boundary concentration for Ptotal used in the model calculation is slightly higher than the measured Ptotal concentration given in Van der Zee et al. (2007) in July and, to a lesser extent, in September. The symbols in (a) represent SPM concentrations obtained from a sediment transport model for average hydrodynamic conditions encountered in the Scheldt estuary (Arndt et al., 2007). The vertical bars are standard deviations. The curves in (a)-(d) correspond to three SPM distributions imposed in the surface complexation model calculations. See text for more details.

tion (Fig. 9d). The latter is apparent when plotting the steady-state profiles of DIP (Fig. 9d) against salinity (Fig. 9a) (see Spiteri et al., 2007). This result reveals that the steady-state DIP distribution is entirely determined by transport in the coastal aquifer. Under transient conditions, there is a net removal of Ptotal from the aquifer by dispersive transport of DIP at the freshwater–seawater interface in both scenarios, potentially followed by export to the coastal zone.

The net removal of Ptotal from the aquifer by seawater intrusion is recorded by the final, steady state distributions of SIP (Fig. 9c and e). For both scenarios, the SIP profiles reveal a zone of enhanced adsorption at intermediate salinities and a zone of desorption at higher salinities. These profiles are generally consistent with the salinity-dependent phosphate adsorption surface shown in Fig. 7b, although a direct comparison is difficult as Ptotal is not constant everywhere within the model domain in time and space.

The predicted phosphate desorption in the model aquifer only results in a relatively small build-up of DIP during the transient phase of seawater intrusion. As proposed by Nyvang (2003) in a study of a Danish coastal aquifer, the intrusion of seawater induces additional biogeochemical changes that affect phosphate cycling. In particular, enhanced microbial sulfate reduction, due to increased sulfate availability and salinity-induced mobilization of dissolved organic matter, may lead to increased DIP production accompanying organic matter mineralization and reduction of ferric iron mineral phases. The latter would result in a loss of adsorption sites for phosphate and therefore cause DIP release. Similarly, Caraco et al. (1989) explain the release of DIP at high sulfate concentration in coastal sediments by the reductive dissolution of ferric iron oxides following

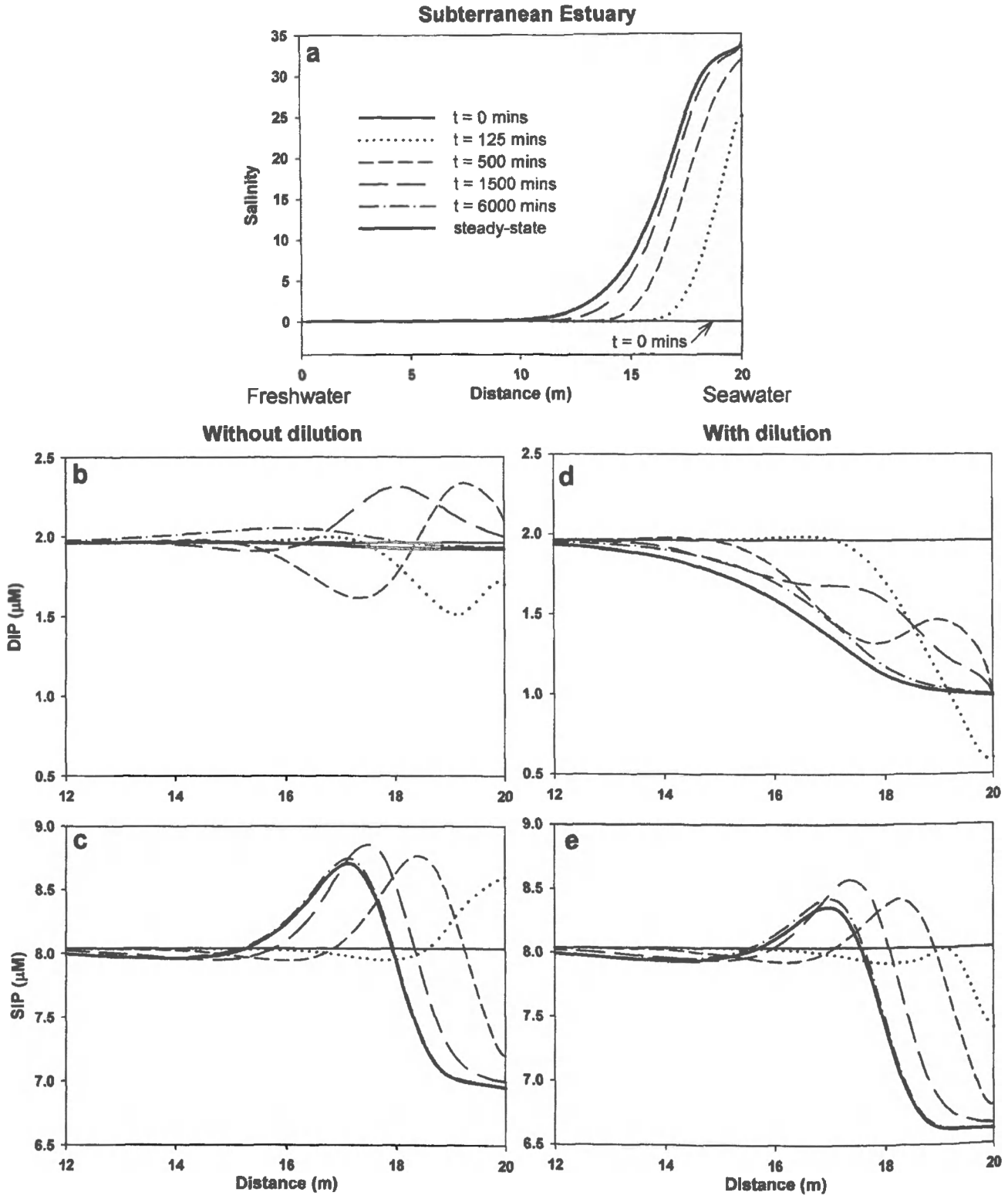

Fig. 9. (a) Time-dependent salinity profiles at mid-depth (5 m) in the model subterranean estuary plotted against longitudinal distance. The coastline is located at 20 m, seawater intrusion starts at time zero. Also shown are the corresponding mid-depth DIP and SIP profiles in the scenarios without (b and c) and with (d and e) dilution. See text for complete discussion.

microbial sulfate reduction, although other authors, for instance Gardolinski et al. (2004), suggest that the release of organic phosphorus can be a major source of the DIP release observed upon salinization. As for the Scheldt estuary, the nature and spatio-temporal distribution of adsorption sites represents a major source of uncertainty when applying the SCM approach to subsurface estuaries.

5. CONCLUSIONS

Phosphate adsorption to mineral particulates in aquatic environments reflects the interplay between non-specific electrostatic interactions, at the mineral surfaces and in solution, and the chemical interactions leading to the formation of aqueous and surface complexes. The surface

Table A.1
pK'_1, pK'_2 and pK'_{HB} as a function of temperature (T) and salinity (S) (from Cai and Wang, 1998; Regnier et al., 2002)

$pK'_1(T,S) = pK'_1(T) + f_1(T).S^{\frac{1}{2}} + f_2(T).S$	$pK'_1(T) = a_0 + \frac{a_1}{T} + a_2 T$	$a_0 = -14.8435$
		$a_1 = 3.40471 \times 10^3$
		$a_2 = 3.2786 \times 10^{-2}$
	$f_1(T) = b_0 + \frac{b_1}{T}$	$b_0 = -2.30848 \times 10^{-2}$
		$b_1 = -14.3456$
	$f_2(T) = c_0 + \frac{c_1}{T}$	$c_0 = 6.91881 \times 10^{-4}$
		$c_1 = 4.29955 \times 10^{-1}$
$pK'_2(T,S) = pK'_2(T) + f_3(T).S^{\frac{1}{2}} + f_4(T).S$	$pK'_2(T) = d_0 + \frac{d_1}{T} + d_2 T$	$d_0 = -6.4980$
		$d_1 = 2.90239 \times 10^3$
		$d_2 = 2.379 \times 10^{-2}$
	$f_3(T) = e_0 + \frac{e_1}{T}$	$e_0 = -4.58898 \times 10^{-1}$
		$e_1 = -41.24048$
	$f_4(T) = g_0 + \frac{g_1}{T}$	$g_0 = 2.84743 \times 10^{-2}$
		$g_1 = -2.55895$
$pK'_{HB}(T,S) = pK'_{HB}(T) + f_5(T).S^{\frac{1}{2}} - f_6(T).S$	$pK'_{HB}(T) = h_0 + \frac{h_1}{T} + h_2 \log(T)$	$h_0 = 1.4802 \times 10^2$
		$h_1 = -8.966 \times 10^3$
		$h_2 = -24.4344$
	$f_5(T) = i_0 + \frac{i_1}{T}$	$i_0 = 0.5998$
		$i_1 = -75.25$
		$j_0 = -1.767 \times 10^{-2}$

complexation model (SCM) describing phosphate binding to the model iron oxide mineral goethite represents a first step in unraveling how this interplay controls the dissolved phosphate levels in surface and subsurface estuaries, that is, in systems characterized by very steep physicochemical gradients of ionic strength, pH, and major ion composition.

Even though phosphate adsorption to ferric iron (hydr)oxides decreases with increasing pH, the magnitude of desorption due to the combined effect of pH and ionic strength alone appears too limited to explain the observed non-conservative behavior of phosphate during freshwater–seawater mixing. In particular, the formation of ternary Mg-phosphate surface complexes acts to limit the extent of phosphate desorption with increasing salinity. A major, and often poorly known, forcing function of phosphate adsorption in estuarine mixing zones is the nature and distribution of surface sites to which phosphate can bind. The model results clearly illustrate that extensive desorption of phosphate in surface estuaries requires the seaward decrease in adsorption capacity to exceed the effects of dilution and potential enhanced binding through formation of ternary Mg-phosphate surface complexes.

Phosphate adsorption and desorption behavior in surface and subterranean estuaries is fundamentally different, because of the different salinity-pH relationships in both settings, but also because the sorbing phase, which is transported with the flow in surface estuaries, is part of the solid matrix in a groundwater system. Hence, the direct extrapolation of field results on phosphate dynamics in surface estuaries to subterranean conditions should be performed with care.

ACKNOWLEDGMENTS

The authors would like to sincerely thank the Associate Editor, Dr. Tim Shaw and four anonymous reviewers for their valuable comments which greatly improved the quality of this manuscript. The authors further wish to acknowledge Dr. Christof Meile (University of Georgia) for making the 2D density-dependent groundwater model available to them. Dr. Meile and Dr. Caroline Slomp (Utrecht University) are also thanked for their interest in this study. Financial support was provided by the Netherlands Organisation for Scientific Research (NWO, Pioneer Program).

APPENDIX. CALCULATION OF DISSOLVED INORGANIC CARBON AND ALKALINITY ALONG THE PH/SALINITY ESTUARINE GRADIENT

In estuarine systems, the total alkalinity (Alk_T) is the sum of Alk_C and the borate alkalinity:

$$Alk_T = Alk_C + \frac{B_T}{K'_{HB}} \quad (A1)$$

where K'_{HB} is the apparent dissociation constant of boric acid. B_T(M), the total boron concentration, is related to salinity (S) as follows (Millero and Sohn, 1992):

$$B_T = 1.2 \times 10^{-5} \cdot S \quad (A2)$$

The freshwater and seawater DIC and Alk_T are mixed conservatively, and the pH along the salinity gradient is computed by numerically solving the following cubic equation (Millero and Sohn, 1992):

$$[H^+]^3 + [H^+]^2\left\{\frac{[K'_1(A-1) + K'_{HB}(A-B)]}{A}\right\} + [H^+]\left\{\frac{K'_1K'_{HB}(A-B-1) + K'_1K'_2(A-2))}{A}\right\} + K'_1K'_2K'_{HB}\frac{(A-B-2)}{A} = 0 \quad (A3)$$

where $A = \frac{Alk_T}{DIC}$ and $B = \frac{B_T}{DIC}$, while K'_1 and K'_2 are the apparent dissociation constants of H_2CO_3 and HCO_3^-, which depend on T and S. The expressions used to compute the values of K'_1, K'_2 and K'_{HB} at different salinities are given in Table A.1.

REFERENCES

Abril G., Etcheber H., Delille B., Frankignoulle M. and Borges A. V. (2003) Carbonate dissolution in the turbid and eutrophic Loire estuary. *Mar. Ecol. Progr. Ser.* **259**, 129–138.

Antelo J., Avena M., Fio S., Lòpez R. and Arce F. (2005) Effects of pH and ionic strength on the adsorption of phosphate and arsenate at the goethite–water interface. *J. Colloid Interface Sci.* **285**, 476–486.

Arndt S., Vanderborght J. P. and Regnier P. (2007) Diatom growth response to physical forcing in a macrotidal estuary: coupling hydrodynamics, sediment transport and biogeochemistry. *J. Geophys. Res.* **112**, C05045. doi:10.1029/2006JC003581.

Atlas E., Culberson C. and Pytkowicz R. M. (1976) Phosphate association with Na^+, Ca^{2+} and Mg^{2+} in seawater. *Mar. Chem.* **4**, 243–254.

Barrow N. J., Bowden J. W., Posner A. M. and Quirk J. P. (1980) Describing the effects of electrolyte on adsorption of phosphate by a variable charge surface. *Aust. J. Soil Res.* **18**, 395–404.

Brasse S., Nellen M., Seifert R. and Michaelis W. (2002) The carbon dioxide system in the Elbe estuary. *Biogeochemistry* **59**, 25–40.

Cai W-J. and Wang Y. (1998) The chemistry, fluxes and sources of carbon dioxide in the estuarine waters of the Satilla and Altamaha Rivers, Georgia. *Limnol. Oceanogr.* **43**, 657–668.

Cai W-J. (2003) Riverine inorganic carbon flux and rate of biological uptake in the Mississippi River plume. *Geophys. Res. Lett.* **30**, 1032. doi:10.1029/2002GL016312.

Caraco N. F., Cole J. J. and Likens G. E. (1989) Evidence for sulphate-controlled phosphorus release from sediments of aquatic systems. *Nature* **341**, 316–318.

Carpenter P. D. and Smith J. D. (1984) Effect of pH, iron and humic acid on the estuarine behaviour of phosphate. *Environ. Tech. Lett.* **6**, 65–72.

Carritt D. E. and Goodgal S. (1954) Sorption reactions and some ecological implications. *Deep-Sea Res.* **1**, 224–243.

Charette M. A., Sholkovitz E. R. and Hansel C. (2005) Trace element cycling in a subterranean estuary: Part 1. Geochemistry of the permeable sediments. *Geochim. Cosmochim. Acta* **69**, 2095–2109.

Cornell R. M. and Schwertmann U. (2003) *The iron oxides: structure, properties, reactions, occurrences and uses*. Wiley, VCH, Weinheim.

Davies C. W. (1938) The extent of dissociation of salts in water: VII. An equation for the mean ionic activity coefficient of an electrolyte in water, and a revision of the dissociation constant of some sulfates. *J. Chem. Soc. PT* **2**, 2093–2098.

Davis, J.A. and Kent, D.B. 1990. Surface complexation modeling in aqueous geochemistry, in: M.F. Hochella and A.F. White (Eds.), Mineral–Water Interface Geochemistry, Rev. Mineral, vol. 23.

De la Paz M., Gómez-Parra A. and Forja J. (2007) Inorganic carbon dynamic and air water CO_2 exchange in the Guadalquivir Estuary (SW Iberian Peninsula). *J. Mar. Sys.* **68**, 265–277.

Devol A. H., Quay P. E., Richey J. E. and Martinelli L. A. (1987) The role of gas exchange in the inorganic carbon, oxygen, and 222Rn budgets of the Amazon River. *Limnol. Oceanogr.* **32**, 235–248.

Dzombak J. A. and Morel F. M. M. (1990) *Surface Complexation Modeling*. Wiley, New York.

Elbaz-Poulichet F., Morley N. H., Cruzado A., Velasquez Z., Achterberg E. P. and Braungardt C. B. (1999) Trace metal and nutrient distribution in an extremely low pH (2.5) river-estuarine system, the Ria of Huelva (South-West Spain). *Sci. Tot. Env.* **227**, 73–83.

Festa J. F. and Hansen D. V. (1976) Turbidity maxima in partially mixed estuaries: a two-dimensional numerical model. *Estuarine Coastal Mar. Sci.* **7**, 347–359.

Fox L. E., Sager S. L. and Wofsy S. C. (1986) The chemical control of soluble phosphorus in the Amazon estuary. *Geochim. Cosmochim. Acta* **50**, 783–794.

Froelich P. N. (1988) Kinetic control of dissolved phosphate in natural rivers and estuaries: a primer on the phosphate buffer mechanism. *Limnol. Oceanogr.* **33**, 649–668.

Frossard E., Brossard M., Hedley M. J. and Metherell A. (1995) Reactions controlling the cycling of P in soils. In *Phosphorus in the Global Environment* (ed. H. Tiessen). John Wiley & Sons.

Gao Y. and Mucci A. (2001) Acid base reactions, phosphate and arsenate complexation, and their competitive adsorption at the surface of goethite in 0.7 M NaCl solution. *Geochim. Cosmochim. Acta* **65**, 2361–2378.

Gao Y. and Mucci A. (2003) Individual and competitive adsorption of phosphate and arsenate on goethite in artificial seawater. *Chem. Geol.* **199**, 91–109.

Gardolinski P. C. F. C., Worsfold P. J. and McKelvie I. D. (2004) Seawater induced release and transformation of organic and inorganic phosphorus from river sediments. *Water Res.* **38**, 688–692.

Geelhoed J. S., Hiemtra T. and Van Riemsdijk W. H. (1997) Phosphate and sulfate adsorption on goethite: single anion and competitive adsorption. *Geochim. Cosmochim. Acta* **61**, 2389–2396.

Goldberg S. and Sposito G. (1984) A chemical model of phosphate adsorption by soils I. Reference oxide minerals. *Soil Sci. Soc. Am. J.* **48**, 772–778.

Hawke D., Carpenter P. D. and Hunter K. A. (1989) Competitive adsorption of phosphate on goethite in marine electrolytes. *Environ. Sci. and Technol.* **23**, 187–191.

Hellings L., Dehairs F., Van Damme S. and Baeyens W. (2001) Dissolved inorganic carbon in a highly polluted estuary (the Scheldt). *Limnol. Oceanogr.* **46**, 1406–1414.

Hiemstra T. and Van Riemsdijk W. H. (1996) A surface structural approach to ion adsorption: the charge distribution (CD) model. *J. Colloid Interface Sci.* **179**, 488–508.

Howland R. J. M., Tappin A. D., Uncles R. J., Plummer D. H. and Bloomer N. J. (2000) Distributions and seasonal variability of pH and alkalinity in the Tweed Estuary, UK. *Sci. Total Environ.*(251/252), 125–138.

Hyacinthe C. and Van Cappellen P. (2004) An authigenic iron phosphate phase inestuarine sediments: composition, formation and chemical reactivity. *Mar. Chem.* **91**, 227–251.

Krom M. D. and Berner R. A. (1980) Adsorption of phosphate in anoxic marine sediments. *Limnol. Oceanogr.* **25**, 797–806.

Lebo M. E. (1991) Particle-bound phosphorus along an urbanized coastal plain estuary. *Mar. Chem.* **34**, 225–246.

Lützenkirchen J. (1999) The constant capacitance model and variable ionic strength: an evaluation of possible applications and applicability. *J. Colloid Interface Sci.* **217**, 8–18.

Meile, C. and Tuncay, K. 2003. RTFEM-Manual, version 8f: Background in finite elements and use of RT.

Millero F. J. (1982) Use of models to determine ionic interactions in natural waters. *Thalass. Jugosl.* **18**, 253–291.

Millero F. J. and Schreiber D. R. (1982) Use of the ion pairing model to estimate activity coefficients of the ionic components of natural waters. *Am. J. Sci.* **282**, 1508–1540.

Millero F. J. and Sohn M. L. (1992) *Chemical Oceanography*. CRC Press, Boca Raton.

Mook W. G. and Koene B. K. S. (1975) Chemistry of dissolved inorganic carbon in estuarine and coastal brackish waters. *Estuarine Coastal Mar. Sci.* **3**, 325–336.

Moore W. S. (1999) The subterranean estuary: a reaction zone of groundwater and sea water. *Mar. Chem.* **65**, 111–125.

Morel F. M. M. and Hering J. G. (1993) *Principles and Applications of Aquatic Chemistry*. Wiley, New York.

Nyvang, V. 2003. Redox processes at the salt-/freshwater interface in an anaerobic aquifer. Ph.D. thesis, Technical Univ. of Denmark.

Paludan C. and Morris J. T. (1999) Distribution and speciation of phosphorus along the salinity gradient in intertidal marsh sediments. *Biogeochemistry* **45**, 197–221.

Press W., Flannery B., Teukolsky S. and Vetterling W. (1992) *Numerical Recipes in Fortran 77: The Art of Scientific Computing*. University Press, Cambridge.

Regnier P., Wollast R. and Steefel C. I. (1997) Long-term fluxes of reactive species in macrotidal estuaries: estimates from a fully transient, multicomponent reaction-transport model. *Mar. Chem.* **58**, 127–145.

Regnier P., O'Kane J. P., Steefel C. I. and Vanderborght J. P. (2002) Modeling complex multi-component reactive-transport systems: towards a simulation environment based on the concept of a knowledge base. *Appl. Math. Modelling* **26**, 913–927.

Schindler P. W. and Stumm W. (1987) Chemical processes at the particle–water interface. In *Aquatic Surface Chemistry* (ed. W. Stumm). Wiley, New York.

Sigg L. and Stumm W. (1981) The interaction of anions and weak acids with the hydrous goethite (α-FeOOH) surface. *Colloids Surf.* **2**, 101–117.

Simpson M. J. and Clement T. P. (2003) A theoretical analysis of the worthiness of Henry and Elder problems as benchmarks of density-dependent groundwater flow models. *Adv. Wat. Res.* **40**, W01504. doi:10.1029/2003WR002199.

Slomp C. P., Van der Gaast S. J. and Van Raaphorst W. (1996) Phosphorus binding by poorly crystalline iron oxides in North Sea sediments. *Mar. Chem.* **52**, 55–73.

Spiteri C., Regnier P., Slomp C. P. and Charette M. A. (2006) pH-Dependent iron oxide precipitation in a subterranean estuary. *J. Geochem. Explor.* **88**, 399–403.

Spiteri C., Van Cappellen P., Regnier P., Meile C. and Slomp C. P. (2007). Phosphate mobilization in coastal aquifers due to seawater intrusion: a model assessment. In *Proceedings of the Groundwater Quality 2007: Securing Groundwater Quality in Urban and Industrial Environments International Conference*. Fremantle, Western Australia.

Spiteri C., Slomp C. P., Tuncay K. and Meile C. (2008) Modeling biogeochemical processes in subterranean estuaries: the effect of flow dynamics and redox conditions on submarine groundwater discharge. *Water Resour. Res.* **44**, W02430. doi:10.1029/2007WR006071.

Stollenwerk K. G. (1996) Simulation of phosphate transport in sewage-contaminated groundwater, Cape Cod, Massachusetts. *Appl. Geochem.* **11**, 317–324.

Stumm W. (1992) *Chemistry of Solid–Water Interface. Processes at the mineral–water and particle–water interface in natural systems*. Wiley, New York.

Sundareshwar P. V. and Morris J. T. (1999) Phosphorus sorption of intertidal marsh sediments along an estuarine salinity gradient. *Limnol. Oceanogr.* **44**, 1693–1701.

Uncles R. J. and Stephens J. A. (1993) The freshwater–saltwater interface and its relationship to the turbidity maximum in the Tamar Estuary, United Kingdom. *Estuaries* **16**, 126–141.

Van der Zee C., Roberts D. R., Rancourt D. G. and Slomp C. P. (2003) Nanogoethite is the dominant reactive oxyhydroxide phase in lake and marine sediments. *Geology* **31**, 993–996.

Van der Zee, C., Roevros, N. and Chou, L. 2007. Phosphorus speciation, transformation and retention in the Scheldt estuary (Belgium/The Netherlands) from the freshwater tidal limits to the North Sea. Mar. Chem. doi:10.1016/j.marchem.2007.01.003.

Vanderborght J. P., Wollast R., Loijens M. and Regnier P. (2002) Application of a transport-reaction model to the estimation of biogases fluxes in the Scheldt estuary. *Biogeochemistry* **1-2**, 207–237.

Vanderborght J. P., Folmer I., Aguilera D., Uhrenholt T. and Regnier P. (2007) Reactive-transport modelling of a river-estuarine coastal zone system: application to the Western Scheldt. *Mar. Chem.* **106**, 92–110.

Wollast R. (1982) Methodology of research in micropollutants—heavy metals. *Water Sci. Technol.* **14**, 107–125.

Wollast R. (1988) The Scheldt estuary. In *Pollution of the North Sea: An Assessment* (eds. W. Salomons, B. Bayne, E. K. Duursma and U. Forstener). Springer, Berlin.

Zhai W., Dai M. and Guo X. (2007) Carbonate system and CO_2 degassing fluxes in the inner estuary of Changjiang (Yangtze) River. *China Mar. Chem.* **107**, 342–356. doi:10.1016/j.marchem.2007.02.011.

Zwolsman J. J. G. (1994) Seasonal variability and biogeochemistry of phosphorus in the Scheldt Estuary, South-West Netherlands. *Estuarine, Coastal Shelf Sci.* **39**, 227–248.

Associate editor: Timothy J. Shaw